The Journal of Physical Chemistry Letters

Letter

Cite This: J. Phys. Chem. Lett. 2017, 8, 5378-5384

pubs.acs.org/JPCL

Stabilization of the Cubic Crystalline Phase in Organometal Halide Perovskite Quantum Dots via Surface Energy Manipulation

Som Sarang,[†] Sara Bonabi Naghadeh,[‡] Binbin Luo,[‡,⊥] Parveen Kumar,[†] Edwin Betady,[§] Vincent Tung,[∥] Michael Scheibner,[†] Jin Z. Zhang,[‡] and Sayantani Ghosh*[,†]

[†]School of Natural Sciences, University of California, Merced, California 95340, United States

[‡]Department of Chemistry and Biochemistry, University of California, Santa Cruz, California 95064, United States

[§]Department of Aerospace Engineering, California State Polytechnic University, Pomona, California 91768, United States

[∥]School of Engineering, University of California, Merced, California 95340, United States

Supporting Information

ABSTRACT: Surface functionalization of nanoscale materials has a significant impact on their properties. We have demonstrated the effect of different passivating ligands on the crystal phase of organometal halide perovskite quantum dots (PQDs). Using static and dynamic spectroscopy, we studied phase transitions in $CH_3NH_3PbBr_3$ PQDs ligated with either octylaminebromide (P-OABr) or 3-aminopropyl triethoxysilane (P-APTES). Around 140 K, P-OABr underwent a structural phase transition from tetragonal to orthorhombic, established by the emergence of a higher energy band in the photoluminescence (PL) spectrum. This was not observed in P-APTES, despite cooling down to 20 K. Additionally, time-resolved and excitation power-dependent PL, as well as Raman spectroscopy over a range of 300−20 K, revealed that recombination rates and types of charge carriers involved are significantly different in P-APTES and P-OABr. Our findings highlight how aspects of PQD phase stabilization are linked to nanoscale morphology and the crystal phase diagram.

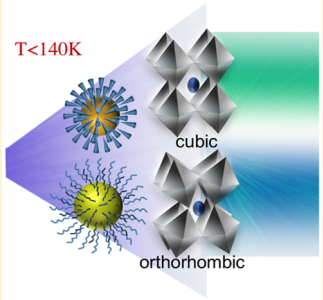

Over the past decade, organometal halide (OMH) based perovskite materials have been extensively researched as promising candidates for photovoltaic and other optoelectronic applications, such as light-emitting diodes (LEDs).[1−7] Following the excellent performance of single-crystal samples and polycrystalline thin films, research efforts have broadened to investigate perovskite nanocrystals, also referred to as perovskite quantum dots (PQDs).[8−10] These studies have shown that, with typically high quantum yield and versatility regarding bandgap tuning within the visible spectrum, PQDs are ideal materials for use in LEDs, lasers, biomedical applications, and optical sensors.[11−13] They have demonstrated good amplified spontaneous emission (ASE) response, with thresholds as low as 220 nJ/cm^2, narrow spectral width, and high output intensity.[14] Aside from device applications, PQDs have also served as ideal platforms to study the aspect of chemical instability that plagues perovskites and has hindered the widespread implementation of perovskite solar cells, despite thin films demonstrating a higher power conversion efficiency than existing silicon solar cells.[15] These many desirable properties in PQDs have not translated into the expected high performance metrics, particularly when compared to their thin film counterparts, although they have the potential to outperform them. For example, perovskite thin film-based LED devices have reported external quantum efficiencies (EQEs) of 3.5 and 8.5% for infrared and green wavelengths,[16] respectively, and with higher exciton binding energy, PQDs should have higher EQEs. However, the highest reported EQE is ∼1%, far less than expected, attributed to incomplete surface passivation and poor charge transport in PQD films.[16] Similarly, while hybrid perovskite thin films have demonstrated optical efficiency of ∼30% as luminescent solar concentrators, one of the highest reported in the field, PQD-based concentrators have only achieved 6%, a result of fluorescence quenching when deposited within polymer matrixes, again a consequence of incompatible surface properties.[17,18]

It is well-known that surfaces of nanocrystals have several charge trap states, arising either from intrinsic defects or from differences in the local environment when compared to the bulk, leading to accumulation of surface charges and thus driving charge carrier migration.[19] Therefore, surface passivation of PQDs using appropriate ligands is necessary to minimize surface trap-related recombination and to improve and sustain fluorescence quantum yield. There have been successful reports of capping PQDs with linear straight chain ligands such as octylamine (OA) and octylaminebromide (OABr), but these synthesis approaches have led to nonuniform structures with variation in morphologies due to the rapid delivery of monomers, resulting from minimal steric hindrance of the capping layer.[9] The use of branched ligands has partly resolved this issue, leading to spherical morphology with higher uniformity. Additionally, computational results have indicated

Received: September 8, 2017
Accepted: October 18, 2017
Published: October 18, 2017

DOI: 10.1021/acs.jpclett.7b02399
J. Phys. Chem. Lett. 2017, 8, 5378−5384

that capping ligands can improve the chemical stability of PQDs, and ligand-dependent variation in morphology and surface properties has been experimentally linked to PQD crystal stability in our prior work.[9]

Methylammonium lead bromide ($CH_3NH_3PbBr_3$) PQDs with a linear (OABr) or a branched (APTES) ligand have been synthesized using a dissolution−precipitation method.[9] Both types of dots are stabilized in the crystalline α cubic structure at room temperature. Under ideal conditions, to maintain high cubic symmetry, the tolerance factor t of the crystal should be close to unity.[20] A deviation from this value will lead to crystal distortions and crystal structures with lower symmetry. Density functional theory calculations have shown the α cubic phase to be the most unstable as it is difficult to satisfy the $t = 1$ condition, and hence, iodide-based perovskite thin films exist in the cubic phase only at a temperature greater than 330 °C.[20] However, bromide-based perovskite crystals do exist in a pseudocubic phase at room temperature due to the difference in the ionic radii of Br^- and I^-, with the smaller Br^- helping in stabilizing the cubic lattice.[21] Interestingly, the phase diagram is also tunable by crystal size, as evident from the fact that iodide-based PQDs exist in the cubic phase at room temperature.[22] Further, in the quest for improved stability and performance of perovskite-based devices, the crystal phase plays an important role. Substitution of methylammonium (MA) with formamidinium (FA) enhances chemical stability considerably, but FA-based perovskite crystals have a phase transition to the yellow nonperovskite polymorph (δ-phase), very close to photovoltaic operational temperatures, making the performance unpredictable.[23] The current route has been to adopt multi-cation synthesis, such as MA/FA or FA/cesium (Cs), with the goal of optimizing both performance and stability, the latter focusing on arresting the phase transition.[2,24]

In this work, we report phase stabilization in PQDs, manifesting as a consequence of morphological and surface ligation differences in PQDs. This results in a difference in surface energy contribution toward the enthalpy of formation of the PQDs, leading to an altered crystal phase diagram compared to the bulk and thin film counterparts. Room-temperature photoluminescence (PL) spectra confirm a bandgap around 530 nm, with a spectral full width at half-maximum (fwhm) of 135 meV. However, below 150 K, while a low-wavelength peak emerges in the PL signal at 470 nm for the PQDs functionalized with OABR (termed P-OABr), no such peak is observed in the ones with APTES (termed P-APTES). This high-energy peak is attributed to the low-temperature transition to the orthorhombic crystal phase, typical of OMH perovskites. Unlike P-OABr, P-APTES appears to be arrested in the high-temperature cubic phase with no apparent transition at temperatures as low as 20 K. We further validate phase transition in P-OABr using temperature-dependent Raman scattering, with P-OABr exhibiting phonon modes below 150 K, whereas P-APTES shows no sharp features indicating the persistence of the Raman-inactive cubic phase. The presence of two phases can have detrimental effects on the performance of the PQDs due to charge transfer between the two phases, loss of monochromaticity, and reduction in recombination lifetime.[25] Our investigation, therefore, not only pertains to improving the optoelectronic properties of PQDs but also has far-reaching consequences for enhancing stability of perovskites in general.

Schematics of the ligands OABr and APTES are shown in Figure 1a,b, along with the functionalized PQDs, referred to as

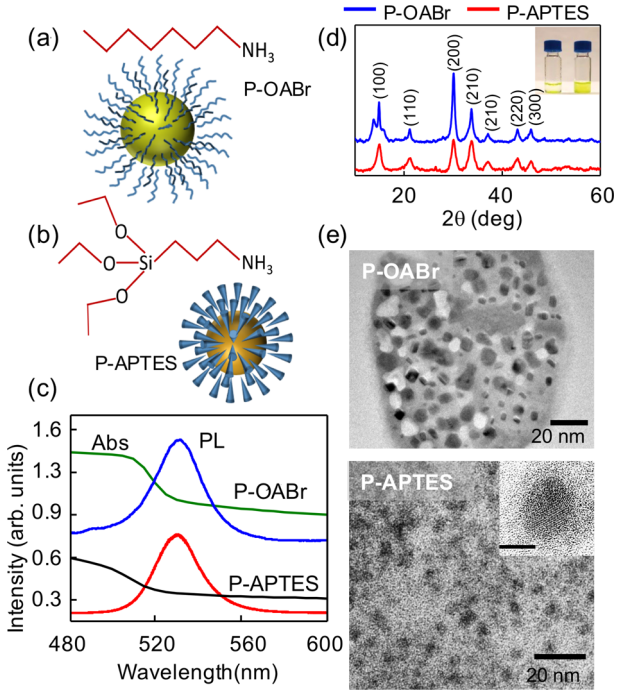

Figure 1. Schematics of ligand molecules and corresponding functionalized PQDs with (a) OABr, referred to as P-OABr, and (b) APTES, designated P-APTES. (c) Absorption and emission spectra for P-OABr and P-APTES at room temperature. (d) XRD confirming the cubic phase of the quantum dots at room temperature with relevant identifying peaks labeled. (e) TEM images of the samples. (bottom, inset) High-resolution TEM image of single P-APTES. The scale bar is 6 nm.

P-OABr and P-APTES, respectively, and the branched structure of APTES is represented as conical appendages on the dot's surface. X-ray diffraction (XRD) patterns of P-OABr and P-APTES shown in Figure 1d have peak positions that confirm the cubic crystal phase of $CH_3NH_3PbBr_3$ at room temperature. Both P-OABr and P-APTES are highly dispersive (inset), remaining stable in solution for almost a week, which we attribute to the high yield of ligand-passivated PQDs obtained through the dissolution−precipitation synthesis route. Transmission electron microscopy (TEM) images in Figure 1e show that while P-OABr has a nonuniform morphology, consisting of both particulate and sheet-like structures, P-APTES has a far more uniform distribution of almost exclusively spherical structures with an average diameter of 6.2 ± 1.5 nm. The amorphous network visible in the background is due to an excess amount of APTES ligand added during synthesis to counter steric factors. An additional high-resolution image is included as an inset as further affirmation of the spherical morphology. The nonuniformity of P-OABr is typical of PQD ensembles and follows as a result of the fast transport of monomers through the capping layer.[9] The higher steric hindrance offered by the branched ligands on P-APTES reduces this transport rate, facilitating uniform shape and size homogeneity. The absorption spectra in Figure 1c show that both PQDs have a characteristic broad spectrum with an excitonic peak centered at 520 nm. The long tails observed at longer wavelengths are due to scattering from the bigger dots in the ensemble.[9] Room-temperature PL spectra of P-OABr and P-APTES in the same figure reveal Gaussian-shaped emission spectra centered at 531 nm with a fwhm of 135 meV. PQDs

DOI: 10.1021/acs.jpclett.7b02399
J. Phys. Chem. Lett. 2017, 8, 5378−5384

have Bohr radii ranging between 1.2 and 4 nm, smaller in comparison to those of dichalcogenide dots, and as a result, variations in the fwhm are dominated by homogeneous broadening effects.[26,27] Consequently, a phonon energy value of 62 meV in P-OABr can be derived from the variation of the fwhm with decreasing temperature (Figure S1).

The difference in surface functionalization causes intriguing differences in the optical properties of the PQDs as well, arising from their surface energy differences, as borne out in temperature-dependent PL spectroscopy. The PL emission for both P-OABr and P-APTES red shifts with lowering temperature, contrary to conventional semiconductors, a result attributed to the reverse band ordering in perovskite crystals.[20] $CH_3NH_3PbBr_3$ transitions from the room-temperature α cubic phase to tetragonal (~220 K) and orthorhombic (~140 K) phases, and the PL emission of P-OABr red shifts from 531 to 545 nm upon lowering the temperature from 300 to 150 K (Figure S2). However, this linear shift in PL peak with temperature has an observable change of slope at 220 K, which could be an indication of the phase transition from the cubic to tetragonal phase. Yet, obtaining a clear proof of a phase transition using PL measurements alone becomes difficult as the bandgap is similar in the two crystal phases and hence both phases have indistinguishable emission spectra. At temperatures below 140 K, the spectrum of P-OABr has multiple emission bands, a result also observed in perovskite thin films due to the coexistence of both orthorhombic and tetragonal phases.[25] The map in Figure 2a shows a high-energy emission band at 470 nm that arises from the orthorhombic phase owing to its larger bandgap, a low-energy band at 545 nm from the remnant tetragonal inclusions, and a broad band centered at 505 nm, arising from defect and bound exciton emissions in the orthorhombic phase. Figure 2c is a representative spectrum at 40 K.

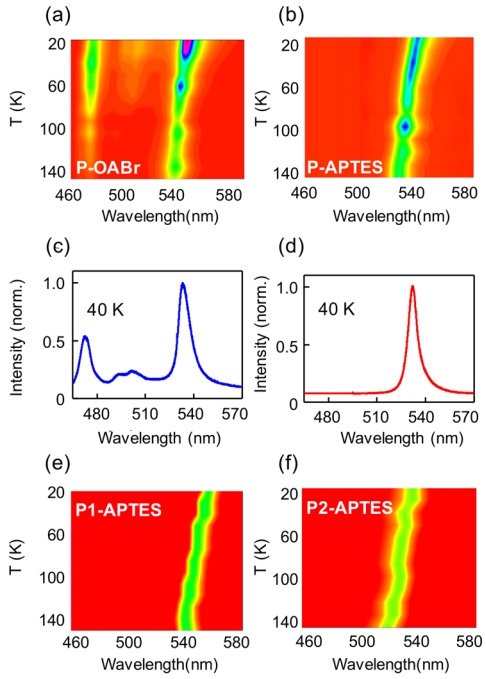

Figure 2. PL intensity mapped with the emission wavelength and temperature for (a) P-OABr and (b) P-APTES. Line cuts of the same maps at 40 K for (c) P-OABr and (d) P-APTES. PL maps of (e) P1-APTES and (f) P2-APTES PQDs ligated with APTES but with larger and smaller diameters than P-APTES.

The most prominent difference in the emission properties of P-OABr and P-APTES at low temperatures is clear in Figure 2b,d. There is no emergence of the high-energy emission peak, indicating that P-APTES remain in the original cubic phase. P-OABr and P-APTES have identical chemical structures before passivation, implying that the origin of this phase stabilization is in the variation of surface energy between the quantum dots due to differences in surface ligands and nanoscale morphology. Our group previously reported the formation of smaller and more uniform spherical PQDs with branched ligand APTES due to slower monomer delivery, while linear ligands lead to a significant percentage of sheet-like structures, some of which can be seen in Figure 1e.[9] Researchers have previously observed such intriguing crystal phase dynamics in MA- and FA-based PQDs, although the underlying reasons have been difficult to identify.[28]

Unlike bulk materials, the surface energy contribution has a more significant perturbation in the Gibbs free energy of nanoparticles and hence plays an important role in determining the crystal phase. By varying the surface energy of nanomaterials, it is possible to attain a thermodynamically stable polymorph of the crystal, otherwise metastable in the bulk. One example is the stabilization of the α-Al_2O_3 phase at room temperature for crystallites smaller than 14 nm, while bulk prefers γ-Al_2O_3.[29] Size-driven effects on structural phases have also been observed in metal oxides like TiO_2 and lanthanides,[30] while low-temperature phase stabilization has been reported in $CsPbI_3$ nanocrystals.[10] Furthermore, bromide-based perovskite crystals have an internal energy difference of 7 kJ/mol between the cubic and orthorhombic crystal phases at room temperature, which can be used as an estimate of the surface energy contribution needed to modify the crystal phase diagram.[31] To further understand the mechanism behind this phase stabilization in P-APTES and uncover any other consequences, we follow up with PL spectroscopy as a function of temperature and include not just P-OABr and P-APTES but additional PQDs of different sizes ligated with APTES, one larger (>10 nm) and one smaller than P-APTES (<3 nm). These are designated P1-APTES and P2-APTES, respectively. As expected, the PL spectrum of the larger quantum dots (P1-APTES) is red shifted, while that of the smaller quantum dots (P2-APTES) is blue shifted compared to that of P-APTES, as shown in Figure 2e,f. Neither of these quantum dots shows the phase transition, implying that the surface energy structural stabilization has contributions from both the nanoscale morphology and surface ligation, unlike the stabilization of the α-Al_2O_3 phase, which solely arises from morphology. The temperature-dependent integrated PL intensity of the PQDs (Figure S3), fit with the Arrhenius equation $I(T) = \frac{I_0}{1 + C_1 \exp\left(-\frac{E_B}{k_B T}\right)}$, allows us to extract their respective exciton binding energies E_B. $I(T)$ and I_0 are integrated PL intensities at temperatures T and 0 K. C_1 is a constant, and k_B is the Boltzmann constant. The fits give values of 105 ± 4.3 meV for P-APTES and 230 ± 7.4 meV for P-OABr. The higher value of the latter is because of the presence of nanosheets in the ensemble.[32]

Given that there could be a small chance that the absence of PL may be a result of trap states, we further probe the phase transition in the PQDs using temperature-dependent Raman

DOI: 10.1021/acs.jpclett.7b02399
J. Phys. Chem. Lett. 2017, 8, 5378−5384

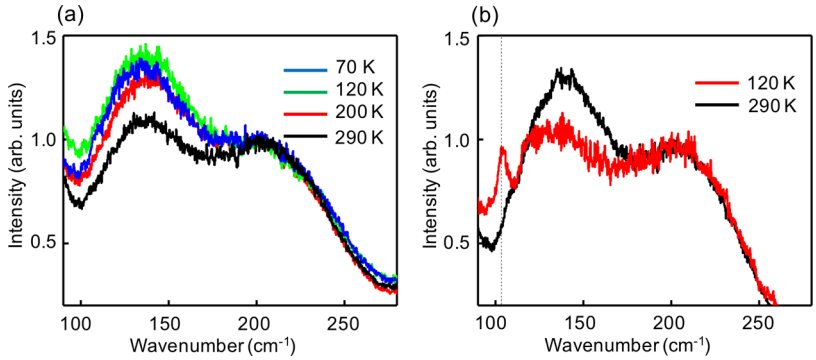

Figure 3. Raman microscopy results for (a) P-APTES and (b) P-OABr with varying temperature. While P-AOBr data show a second emerging peak at 120 K proclaiming the onset of transition to the orthorhombic phase, no such peak is observed in P-APTES.

scattering in the high-frequency region where phonon modes appear, depending on structural symmetry. Intermolecular modes originating from methylamine can serve as an indication of a structural phase transition. As seen in Figure 3a,b, room-temperature Raman scattering of P-APTES and P-OABr can exhibit broad peaks with no significant sharp features, typical for perovskite crystals with cubic phase symmetry, as they have no Raman-active phonon modes present.[33] However, upon lowering the temperature below 120 K, we observed a sharp Raman band for P-OABr at around 105 cm^{-1}, consistent with previous reports of phase transition from tetragonal to orthorhombic phases.[34] On the other hand, no sharp feature in the Raman spectra was observed for P-APTES, even upon lowering the temperature below 70 K, as shown in Figure 3a, confirming that the structure remains arrested in the cubic phase and supporting our conclusion drawn from PL data.

Structural phase transition in perovskite thin films is accompanied by changes in charge carrier behavior, including both the type of carriers that dominate recombination (bimolecular or excitonic) as well the associated time scales. To correlate the phase transition with carrier dynamics, we measured low-temperature time-resolved PL between 290 and 20 K. Given that the calculated E_B for the PQDs is larger than those of thin films, free carrier recombination is suppressed across the entire temperature range. The average lifetimes of exciton decay for P-OABr and P-APTES are calculated by fitting the data in Figure 4a,b to a stretched exponential fit $I(t) = I_0 e^{(t/\tau)^\beta}$, to account for continuous higher-order recombinations.[35] However, even without the benefit of quantitative analysis, a difference between the two trends with temperature is clearly visible. For P-OABr, the results mimic what is observed in thin film samples—a single, long lifetime in the tetragonal phase between 300 and 140 K followed by the emergence of a rapid recombination route when the orthorhombic phase appears.[25] In contrast, the P-APTES time-resolved curves show a continuous and gradual decrease of exciton lifetime with temperature. The values of these recombination times, extracted from fits, are plotted in Figure 4c,d for P-OABr and P-APTES, respectively. They reveal an average lifetime of 2 and 9 ns for the two at room temperature, and the mildly longer value for the P-APTES ensemble is likely a reflection of more homogeneous morphology and size. The dynamics of the low-energy PL in P-OABr in Figure 4c shows a sudden jump in the lifetime at around 210 K, reaching a value of 13.5 ns. It is interesting to note that this occurs at the same temperature where one would expect the cubic to tetragonal phase transition and where such

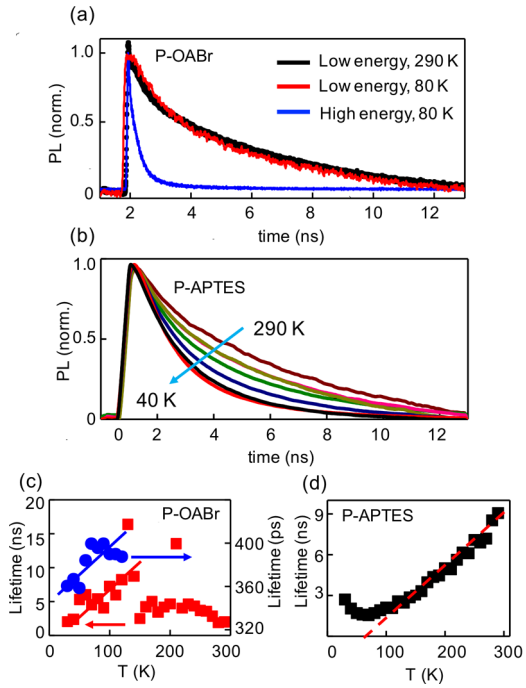

Figure 4. Time-resolved PL curves for (a) P-OABr and (b) P-APTES as functions of temperature. Recombination lifetimes extracted from stretched exponential fits of the two are plotted in (c) and (d), respectively. For P-OABr, the high-temperature, low-energy phase is plotted as squares, and the low-temperature, high-energy orthorhombic phase is represented as circles. All lines in (c) and (d) are guides to the eye.

enhancements in carrier lifetimes can occur due to excessive scattering of excitons at grain boundaries. The lifetime decreases to 4 ns at 190 K, and no big changes are observed until 140 K, where another sudden rise in carrier lifetime is observed, attributed to the phase transition from the tetragonal to orthorhombic phase. As the temperature was reduced further, a gradual decrease in the carrier lifetime was observed. Most colloidal quantum dots show an increase in PL lifetime with lowering temperature due to dominant excitonic emissions. Nevertheless, previous reports have indicated a reverse trend in PQDs where a reduction in charge carrier lifetime with lowering temperature arises from the interactions of free and trapped excitons with surface states or localized states as relaxation pathways.[36]

At around 130 K, the high-energy band emerged with a much shorter lifetime, ~350 ps, compared to the lower-energy band.

DOI: 10.1021/acs.jpclett.7b02399
J. Phys. Chem. Lett. 2017, 8, 5378−5384

This short carrier lifetime has been observed in perovskite thin films for the orthorhombic phase and is attributed to the migration of charge carriers from the higher-energy band to the lower-energy tetragonal inclusions.[25] In the P-OABr dots, an interesting observation is the small contribution of higher-order exponential decay terms in the higher-energy band (evident from β values close to 1), indicating that the charge transfer rate between high- and low-energy bands is at least an order of magnitude faster than the charge recombination rate. The formation of smaller tetragonal inclusions as the temperature was lowered further increased the biexcitonic recombination rate, with a gradual decrease in lifetime of this energy band, down to 300 ps at 40 K. As shown in Figure 4b,d, the time-resolved PL of P-APTES is far less complicated. The charge carrier lifetime continuously decreases as temperature is reduced, bottoming out at 1.4 ns at 70 K, with a small recovery beyond that. The recovery mechanism is still not fully understood but may be related to thermal activation energy for charge transfer to localized centers or surface states previously mentioned.

Finally, we consider the dependence of integrated PL intensity on excitation power in Figure 5. The fit used is a power law, described as $I_{PL} = I_{ex}^{k}$. In direct bandgap semiconductors, $k > 2$ indicates free charge carrier recombination, $1 < k < 2$ for free and bound exciton recombination, and $k \leq 1$ signifies free to bound exciton recombination or the emission from excitons bound to isoelectronic defects or localized states, as observed in the case of silicon.[37,38] Due to the high exciton binding energies in all of our PQDs, we do not expect free carrier recombination to have a significant presence, and this is proven correct. In Figure 5a, P-OABr quantum dots show $k \approx 1$, confirming excitonic recombination, although there is a change of slope at higher powers due to saturation of the localized states involved, particularly at 290 K. In P-APTES, $k = 0.8$ at 290 K, which means that, while recombination is predominantly due to free excitons, there is possibly some contribution from bound excitons. The weight of this latter category increases with decreasing temperature, and we observed $k \approx 0.5$ at 200 and 120 K.

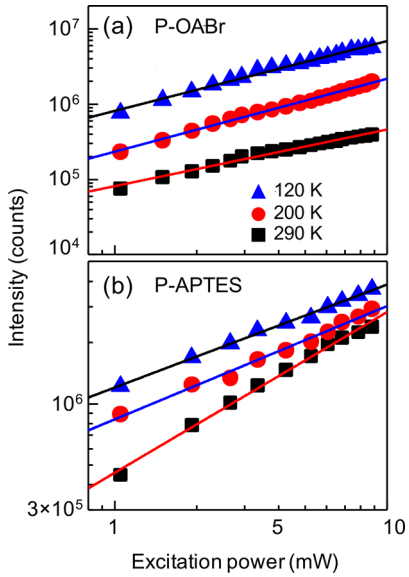

Figure 5. Integrated PL intensity as a function of excitation power at different temperatures for (a) P-OABr and (b) P-APTES. Power law fits are used to identify the type of carriers participating in the emission (explained in the text).

In this work, we have studied the temperature-dependent PL emission of PQDs ligated with two different ligands, OABr and APTES. PL spectra at low temperatures reveal the expected phase transition, from the tetragonal to orthorhombic phase in P-OABr at ~140 K, but no such phase transition was observed in P-APTES, which remained in the cubic phase. We attribute this absence of phase transition to differences in surface energy contributions to their Gibbs free energy, which significantly modifies the crystal phase diagram, leading to an energetically stable crystal cubic phase in P-APTES nanocrystals. This difference in surface energy arises from a difference in the surface ligation and the morphology of PQDs, with APTES favoring the formation of uniform spherical nanostructures. The observed phase stabilization in P-APTES was further demonstrated using Raman spectroscopy and time-resolved PL, which showed a sudden drop in PL recombination lifetime associated with the transition to orthorhombic structure in P-OABr but not in P-APTES. Temperature- and power-dependent PL reveals strictly excitonic recombination over the full temperature range at which measurements are performed, albeit with varying contributory levels from bound and free excitons. Our reported results establish a link between phase stabilization and morphology-related surface stabilization of PQDs. This opens up new possibilities of phase stabilization in other quantum dot systems using appropriate ligands and provides insights into proposing new routes for the stabilization of perovskite crystals.

■ EXPERIMENTAL METHODS

PQDs are synthesized using previously reported methods by our groups.[8,9] Detailed description of the synthesis process and an affirmation of surface ligation can be found in ref 9. Samples for low-temperature PL were prepared by drop-casting 2 μL of the PQDs in toluene onto clean glass slides and subsequently drying. For optical measurements, we used two excitation sources: a tunable, pulsed ultrafast laser (MIRA 900) with a repetition rate of 76 MHz and continuous-wave (CUBE) laser emitting at 409 nm. The PL data were taken using an Acton 300i spectrometer and then dispersed onto a thermoelectrically cooled charge-coupled device (CCD) with a spectral resolution of 0.18 nm. For time-resolved PL measurements, we used a time-correlated single-photon counting (TCSPC) system (Picoquant) in conjunction with the pulsed source. The temperature-dependent measurements were done in a cryo-free system from Advanced Research Systems with a base temperature of 10 K. TEM and X-ray powder diffraction were used to demonstrate high crystallinity and attain average PQD size. The P-APTES and P-OABR were carefully dispersed on a silicon substrate to perform the Raman scattering measurements. A variable-wavelength continuous wave diode laser source, operated at a wavelength of ~915 nm with a power of ~100 μW, was focused on the sample using a 50× objective. The wavelengths below the bandgap were used to minimize the exciton−phonon interaction. The backscattered light was passed through the same objective and a single stage spectrometer and collected using a liquid-nitrogen-cooled CCD camera. The slit width of the single spectrometer was set at 100 μm. All measurements were done in a closed-cycle helium-cooled cryostat at a temperature of 70−300 K.

DOI: 10.1021/acs.jpclett.7b02399
J. Phys. Chem. Lett. 2017, 8, 5378−5384

■ ASSOCIATED CONTENT

Supporting Information

The Supporting Information is available free of charge on the ACS Publications website at DOI: 10.1021/acs.jpclett.7b02399.

Additional information regarding the temperature-dependent line width, phonon energy fits, PL map varying with temperature between 300 and 150 K in P-APTES, and extraction of the activation energy from an Arrhenius fit to the PL intensity versus temperature graph (PDF)

■ AUTHOR INFORMATION

Corresponding Author

*E-mail: sghosh@ucmerced.edu.

ORCID

Jin Z. Zhang: 0000-0003-3437-912X

Sayantani Ghosh: 0000-0003-3440-7194

Present Address

⊥B.L.: Department of Chemistry, Shantou University, Guangdong 515063, China.

Notes

The authors declare no competing financial interest.

■ ACKNOWLEDGMENTS

This work was supported by NASA MIRO Grant No. NNX15AQ01A. P.K. and M.S. also acknowledge funding by the Defense Threat Reduction Agency (Award No. HDTRA1-15-1-0011) and the Air Force Office of Scientific Research (Award No. FA9550-16-1-0278). S.S. acknowledges funding from the Southern California Edison Fellowship.

■ REFERENCES

(1) Nie, W.; Tsai, H.; Asadpour, R.; Blancon, J.-C.; Neukirch, A. J.; Gupta, G.; Crochet, J. J.; Chhowalla, M.; Tretiak, S.; Alam, M. A.; et al. High-Efficiency Solution-Processed Perovskite Solar Cells with Millimeter-Scale Grains. *Science* **2015**, *347*, 522−525.

(2) Saliba, M.; Matsui, T.; Seo, J.-Y.; Domanski, K.; Correa-Baena, J.-P.; Nazeeruddin, M. K.; Zakeeruddin, S. M.; Tress, W.; Abate, A.; Hagfeldt, A.; et al. Cesium-Containing Triple Cation Perovskite Solar Cells: Improved Stability, Reproducibility and High Efficiency. *Energy Environ. Sci.* **2016**, *9*, 1989−1997.

(3) Ishihara, H.; Sarang, S.; Chen, Y.-C.; Lin, O.; Phummirat, P.; Thung, L.; Hernandez, J.; Ghosh, S.; Tung, V. Nature Inspiring Processing Route toward High Throughput Production of Perovskite Photovoltaics. *J. Mater. Chem. A* **2016**, *4*, 6989−6997.

(4) Ergen, O.; Gilbert, S. M.; Pham, T.; Turner, S. J.; Tan, M. T. Z.; Worsley, M. A.; Zettl, A. Graded Bandgap Perovskite Solar Cells. *Nat. Mater.* **2016**, *16*, 522−525.

(5) Jeon, N. J.; Noh, J. H.; Yang, W. S.; Kim, Y. C.; Ryu, S.; Seo, J.; Seok, S. Il Compositional Engineering of Perovskite Materials for High-Performance Solar Cells. *Nature* **2015**, *517*, 476−480.

(6) Zhou, H.; Chen, Q.; Li, G.; Luo, S.; Song, T.; Duan, H.-S.; Hong, Z.; You, J.; Liu, Y.; Yang, Y. Photovoltaics. Interface Engineering of Highly Efficient Perovskite Solar Cells. *Science* **2014**, *345*, 542−546.

(7) Ishihara, H.; Chen, W.; Chen, Y.-C.; Sarang, S.; De Marco, N.; Lin, O.; Ghosh, S.; Tung, V. Electrohydrodynamically Assisted Deposition of Efficient Perovskite Photovoltaics. *Adv. Mater. Interfaces* **2016**, *3*, 1500762.

(8) Luo, B.; Pu, Y. C.; Yang, Y.; Lindley, S. A.; Abdelmageed, G.; Ashry, H.; Li, Y.; Li, X.; Zhang, J. Z. Synthesis, Optical Properties, and Exciton Dynamics of Organolead Bromide Perovskite Nanocrystals. *J. Phys. Chem. C* **2015**, *119*, 26672−26682.

(9) Luo, B.; Pu, Y. C.; Lindley, S. A.; Yang, Y.; Lu, L.; Li, Y.; Li, X.; Zhang, J. Z. Organolead Halide Perovskite Nanocrystals: Branched Capping Ligands Control Crystal Size and Stability. *Angew. Chem., Int. Ed.* **2016**, *55*, 8864−8868.

(10) Swarnkar, A.; Marshall, A. R.; Sanehira, E. M.; Chernomordik, B. D.; Moore, D. T.; Christians, J. A.; Chakrabarti, T.; Luther, J. M. Quantum Dot−induced Phase Stabilization of α-CsPbI3 Perovskite for High-Efficiency Photovoltaics. *Science* **2016**, *354*, 92−95.

(11) Shi, Z.; Li, Y.; Zhang, Y.; Chen, Y.; Li, X.; Wu, D.; Xu, T.; Shan, C.; Du, G. High-Efficiency and Air-Stable Perovskite Quantum Dots Light-Emitting Diodes with an All-Inorganic Heterostructure. *Nano Lett.* **2017**, *17*, 313−321.

(12) Huang, H.; Zhao, F.; Liu, L.; Zhang, F.; Wu, X. G.; Shi, L.; Zou, B.; Pei, Q.; Zhong, H. Emulsion Synthesis of Size-Tunable $CH_3NH_3PbBr_3$ Quantum Dots: An Alternative Route toward Efficient Light-Emitting Diodes. *ACS Appl. Mater. Interfaces* **2015**, *7*, 28128−28133.

(13) Kim, Y.; Yassitepe, E.; Voznyy, O.; Comin, R.; Walters, G.; Gong, X.; Kanjanaboos, P.; Nogueira, A. F.; Sargent, E. H. Efficient Luminescence from Perovskite Quantum Dot Solids. *ACS Appl. Mater. Interfaces* **2015**, *7*, 25007−25013.

(14) Zhu, H.; Fu, Y.; Meng, F.; Wu, X.; Gong, Z.; Ding, Q.; Gustafsson, M. V.; Trinh, M. T.; Jin, S.; Zhu, X.-Y. Lead Halide Perovskite Nanowire Lasers with Low Lasing Thresholds and High Quality Factors. *Nat. Mater.* **2015**, *14*, 636−642.

(15) Berhe, T. A.; Su, W.-N.; Chen, C.-H.; Pan, C.-J.; Cheng, J.-H.; Chen, H.-M.; Tsai, M.-C.; Chen, L.-Y.; Dubale, A. A.; Hwang, B.-J. Organometal Halide Perovskite Solar Cells: Degradation and Stability. *Energy Environ. Sci.* **2016**, *9*, 323−356.

(16) Sutherland, B. R.; Sargent, E. H. Perovskite Photonic Sources. *Nat. Photonics* **2016**, *10*, 295−302.

(17) Nikolaidou, K.; Sarang, S.; Hoffman, C.; Mendewala, B.; Ishihara, H.; Lu, J. Q.; Ilan, B.; Tung, V.; Ghosh, S. Hybrid Perovskite Thin Films as Highly Efficient Luminescent Solar Concentrators. *Adv. Opt. Mater.* **2016**, *4*, 2126−2132.

(18) Zhao, H.; Zhou, Y.; Benetti, D.; Ma, D.; Rosei, F. Perovskite Quantum Dots Integrated in Large-Area Luminescent Solar Concentrators. *Nano Energy* **2017**, *37*, 214−223.

(19) Boles, M. A.; Ling, D.; Hyeon, T.; Talapin, D. V. The Surface Science of Nanocrystals. *Nat. Mater.* **2016**, *15*, 141−153.

(20) Yin, W.-J.; Yang, J.-H.; Kang, J.; Yan, Y.; Wei, S.-H. Halide Perovskite Materials for Solar Cells: A Theoretical Review. *J. Mater. Chem. A* **2015**, *3*, 8926−8942.

(21) Sheng, R.; Ho-Baillie, A.; Huang, S.; Chen, S.; Wen, X.; Hao, X.; Green, M. A. Methylammonium Lead Bromide Perovskite-Based Solar Cells by Vapor-Assisted Deposition. *J. Phys. Chem. C* **2015**, *119*, 3545−3549.

(22) Yakunin, S.; Protesescu, L.; Krieg, F.; Bodnarchuk, M. I.; Nedelcu, G.; Humer, M.; De Luca, G.; Fiebig, M.; Heiss, W.; Kovalenko, M. V. Low-Threshold Amplified Spontaneous Emission and Lasing from Colloidal Nanocrystals of Caesium Lead Halide Perovskites. *Nat. Commun.* **2015**, *6*, 8056.

(23) Zheng, X.; Wu, C.; Jha, S. K.; Li, Z.; Zhu, K.; Priya, S. Improved Phase Stability of Formamidinium Lead Triiodide Perovskite by Strain Relaxation. *ACS Energy Lett.* **2016**, *1*, 1014−1020.

(24) Ye, T.; Ma, S.; Jiang, X.; Wei, L.; Vijila, C.; Ramakrishna, S. Performance Enhancement of Tri-Cation and Dual-Anion Mixed Perovskite Solar Cells by Au@SiO2 Nanoparticles. *Adv. Funct. Mater.* **2017**, *27*, 1606545.

(25) Sarang, S.; Ishihara, H.; Chen, Y.-C.; Lin, O.; Gopinathan, A.; Tung, V. C.; Ghosh, S. Low Temperature Excitonic Specroscopy and Dynamics as a Probe of Quality in Hybrid Perovskite Thin Films. *Phys. Chem. Chem. Phys.* **2016**, *18*, 28428.

(26) Liang, Z.; Zhao, S.; Xu, Z.; Qiao, B.; Song, P.; Gao, D.; Xu, X. Shape-Controlled Synthesis of All-Inorganic $CsPbBr_3$ Perovskite Nanocrystals with Bright Blue Emission. *ACS Appl. Mater. Interfaces* **2016**, *8*, 28824−28830.

(27) Sichert, J. A.; Tong, Y.; Mutz, N.; Vollmer, M.; Fischer, S.; Milowska, K. Z.; García Cortadella, R.; Nickel, B.; Cardenas-Daw, C.; Stolarczyk, J. K.; et al. Quantum Size Effect in Organometal Halide Perovskite Nanoplatelets. *Nano Lett.* **2015**, *15*, 6521−6527.

DOI: 10.1021/acs.jpclett.7b02399
J. Phys. Chem. Lett. 2017, 8, 5378−5384

(28) Dai, J.; Zheng, H.; Zhu, C.; Lu, J.; Xu, C. Comparative Investigation on The Temperature-Dependent Photoluminescence of $CH_3NH_3PbBr_3$ and $CH(NH_2)_2PbBr_3$ Microstructures. *J. Mater. Chem. C* **2016**, *4*, 4408−4413.
(29) McHale, J. M.; Navrotsky, A.; Perrotta, A. J. Effects of Increased Surface Area and Chemisorbed H_2O on the Relative Stability of Nanocrystalline γ-Al_2O_3 and α-Al_2O_3. *J. Phys. Chem. B* **1997**, *101*, 603−613.
(30) Wang, F.; Han, Y.; Lim, C. S.; Lu, Y.; Wang, J.; Xu, J.; Chen, H.; Zhang, C.; Hong, M.; Liu, X. Simultaneous Phase and Size Control of Upconversion Nanocrystals through Lanthanide Doping. *Nature* **2010**, *463*, 1061−1065.
(31) Protesescu, L.; Yakunin, S.; Bodnarchuk, M. I.; Krieg, F.; Caputo, R.; Hendon, C. H.; Yang, R. X.; Walsh, A.; Kovalenko, M. V. Nanocrystals of Cesium Lead Halide Perovskites ($CsPbX_3$, X = Cl, Br, and I): Novel Optoelectronic Materials Showing Bright Emission with Wide Color Gamut. *Nano Lett.* **2015**, *15*, 3692−3696.
(32) Zhang, Y.; Liu, J.; Wang, Z.; Xue, Y.; Ou, Q.; Polavarapu, L.; Zheng, J.; Qi, X.; Bao, Q. Synthesis, Properties, and Optical Applications of Low-Dimensional Perovskites. *Chem. Commun.* **2016**, *52*, 13637−13655.
(33) Ledinský, M.; Löper, P.; Niesen, B.; Holovský, J.; Moon, S. J.; Yum, J. H.; De Wolf, S.; Fejfar, A.; Ballif, C. Raman Spectroscopy of Organic-Inorganic Halide Perovskites. *J. Phys. Chem. Lett.* **2015**, *6*, 401−406.
(34) Matsuishi, K.; Ishihara, T.; Onari, S.; Chang, Y. H.; Park, C. H. Optical Properties and Structural Phase Transitions of Lead-Halide Based Inorganic-Organic 3D and 2D Perovskite Semiconductors under High Pressure. *Phys. Status Solidi B* **2004**, *241*, 3328−3333.
(35) Lee, K. C. B.; Siegel, J.; Webb, S. E. D.; Lévêque-Fort, S.; Cole, M. J.; Jones, R.; Dowling, K.; Lever, M. J.; French, P. M. W. Application of the Stretched Exponential Function to Fluorescence Lifetime Imaging. *Biophys. J.* **2001**, *81*, 1265−1274.
(36) Li, J.; Yuan, X.; Jing, P.; Li, J.; Wei, M.; Hua, J.; Zhao, J.; Tian, L. Temperature-Dependent Photoluminescence of Inorganic Perovskite Nanocrystal Films. *RSC Adv.* **2016**, *6*, 78311−78316.
(37) Luckert, F.; Yakushev, M. V.; Faugeras, C.; Karotki, A. V.; Mudryi, A. V.; Martin, R. W. Excitation Power and Temperature Dependence of Excitons in $CuInSe_2$. *J. Appl. Phys.* **2012**, *111*, 093507.
(38) He, H.; Yu, Q.; Li, H.; Li, J.; Si, J.; Jin, Y.; Wang, N.; Wang, J.; He, J.; Wang, X.; et al. Exciton Localization in Solution-Processed Organolead Trihalide Perovskites. *Nat. Commun.* **2016**, *7*, 10896.

DOI: 10.1021/acs.jpclett.7b02399
J. Phys. Chem. Lett. 2017, 8, 5378−5384